

## Article

# A Kinetic Study of Photocatalytic Degradation of Phenol over Titania–Silica Mixed Oxide Materials under UV Illumination

Shivatharsiny Yohi <sup>1,2,\*</sup>, Chia-Ming Wu <sup>2</sup> and Ranjit T. Koodali <sup>3</sup> <sup>1</sup> Department of Chemistry, University of Jaffna, Jaffna 40000, Sri Lanka<sup>2</sup> Department of Chemistry, University of South Dakota, Vermillion, SD 57069, USA; Chia-Ming.Wu@coyotes.usd.edu<sup>3</sup> Department of Chemistry, Western Kentucky University, Bowling Green, KY 42101, USA; ranjit.koodali@wku.edu

\* Correspondence: yshiva@univ.jfn.ac.lk

**Abstract:** A set of titania–silica mixed oxide materials were prepared by a cosolvent-induced gelation method using ethanol and toluene as solvent and cosolvent, respectively. These materials were extensively characterized by utilizing several characterization techniques and assessed for phenol degradation under UV illumination. The degradation of phenol follows first-order kinetics, and fragmented products formed during the phenol degradation were qualitatively identified by using high performance liquid Chromatographic (HPLC) and atomic pressure chemical ionization mass spectroscopic (APCI-MS) techniques. The complete mineralization of phenol was further evidenced by the measurement of the total organic contents that remained in the solution after irradiation. The pore diameter of the materials was found to be the key factor for phenol degradation, whereas surface area and pore volume play a role among the mixed oxide materials. In addition, in the mixed oxide system there was an inverse correlation obtained with the particle size of the materials and the degradation efficiency. The smaller particle size of titania in the mixed oxide material was found to be a requirement for an effective degradation of phenol.

**Keywords:** titania–silica; Phenol; OH radical; HPLC; APCI-mass spectroscopy



**Citation:** Yohi, S.; Wu, C.-M.; Koodali, R.T. A Kinetic Study of Photocatalytic Degradation of Phenol over Titania–Silica Mixed Oxide Materials under UV Illumination. *Catalysts* **2022**, *12*, 193. <https://doi.org/10.3390/catal12020193>

Academic Editors: Faryal Idrees and Faheem K. Butt

Received: 14 January 2022

Accepted: 31 January 2022

Published: 4 February 2022

**Publisher's Note:** MDPI stays neutral with regard to jurisdictional claims in published maps and institutional affiliations.



**Copyright:** © 2022 by the authors. Licensee MDPI, Basel, Switzerland. This article is an open access article distributed under the terms and conditions of the Creative Commons Attribution (CC BY) license (<https://creativecommons.org/licenses/by/4.0/>).

## 1. Introduction

Aquatic pollution is one of the major concerns that directly impact the health of the ecosystem, mainly due to waste mismanagement [1–3]. Toxic organic pollutants generated from industrial processes released directly into the environment eventually affect water worldwide. In addition, these toxic organic pollutants, depending upon their different occurrences in nature, toxicity, and persistence, pose a threat to humans through contamination of drinking water supplies. In particular, phenols and their derivatives are listed as major environmental hazards due to their bio-recalcitrant and acute toxicity in the priority pollutant list by the US Environmental Protection Agency (US-EPA) [4]. The toxicity of phenolic compounds is mainly attributed to the ease with which free electrons contribute to the formation of phenoxy radicals. These radicals can penetrate the cell and damage membranes of the endoplasmic reticulum, mitochondria, and nucleus [5,6]. In addition, the interactions of the hydrophobic type of phenolic compounds are leading to necrosis of the skin, the kidneys, liver, muscle, and eyes [7]. Furthermore, some pollutants, such as drugs, pesticides, persistent organic pollutants (POPs), etc. are found to be a major health concern even at low concentrations, due to their endocrine-disrupting potency. These validate the necessity for the removal of such phenolic contaminants and minimization of their long-term existence and accumulation. Consequently, considerable efforts have been devoted to achieving an effective removal of these pollutants from the polluted aquatic environment. The conventional wastewater purification methods, such as adsorption, membrane filtration, coagulation, and flocculation, generate undesirable secondary waste

pollutants during the process [8–14]. Thus, these methods are not cost effective and are extremely sensitive to several experimental conditions, due to the need for additional steps to completely remove the pollutants.

The advanced oxidation processes (AOP) have been documented as an efficient route for the degradation of wide variety of toxic pollutants [1,15,16]. In particular, the heterogeneous photocatalytic oxidation (HPO) process employing semiconductor materials, such as  $\text{TiO}_2$  in the presence of UV irradiation, has been utilized as an effective method to mineralize the persistent organic pollutants (POPs) and produce biodegradable and less toxic substances, such as  $\text{CO}_2$  and  $\text{H}_2\text{O}$ . The highly active hydroxyl ( $\bullet\text{OH}$ ) radicals formed during the heterogeneous process are the key elements for the conversion of a wide spectrum of toxic organic compounds into relatively innocuous end products. Even though  $\text{TiO}_2$  has been considered as an effective semiconductor in the heterogeneous technique due to its photostability and hydrophilic nature, the application of the  $\text{TiO}_2$ -mediated photodegradation presents several technical challenges that include inefficient visible light harvesting, catalyst deactivation due to the rapid recombination of the electron-hole pairs generated during the irradiation process, and the separation of the  $\text{TiO}_2$  catalyst after water treatment [17]. Thus, to overcome these challenges, mixed oxide semiconductor materials containing  $\text{TiO}_2$  as an active center have been explored and utilized for the mineralization of organics [18–22]. In particular, titania loaded on a silica support has gained more attention due to the durability and high surface area of silica [23]. These materials have proven to be better catalysts for the photo-induced mineralization of organic and inorganic pollutants [24–29]. In this regard, we have developed a cosolvent-induced gelation method to prepare mixed titania–silica materials with an equimolar ratio of Ti:Si [30] and explored their potential in the degradation of organic pollutants [31,32]. As an extension of the previous work, we have altered the titania–silica ratio in the synthesis route to prepare a set of materials with a different Ti:Si composition and harness them for phenol degradation in this study.

The degradation of phenol or phenolic compounds depends on several factors that include the following; the solution pH, concentration and type of organic substrate, light intensity, oxidant concentration, composition of catalysts, and calcination temperatures, which have been investigated in various reports [33–35]. However, the scarcity of reports may be due to the competitive and collective effect of the physicochemical properties of the photocatalyst against the activity. To the best of our knowledge, only one report [36] explains the differences in the activity of phenol degradation with a series of materials prepared with the different composition of titania–silica. Even though the previous reports linked the structural properties and the effective mineralization, the followings points are identified as major gaps in the existing literature: (i) systematic variation in the titania–silica composition for the preparation of  $\text{TiO}_2$ – $\text{SiO}_2$  aperiodic mixed oxide materials prepared by the sol–gel method, (ii) an extensive characterization of the textural properties of the  $\text{TiO}_2$ – $\text{SiO}_2$  materials, (iii) a detailed study on the effect of textural properties of the  $\text{TiO}_2$ – $\text{SiO}_2$  materials for the photocatalysis, (iv) comprehensive identification of mineralized aromatic and carboxylic acid by-products during the phenol photodegradation over titania–silica mixed oxide materials using mass spectroscopic analysis, and (v) the role of hydroxyl radical in the degradation rate.

Thus, this study mainly aims to evaluate and summarize the influence of different titania–silica compositions on the textural properties of the materials and their degradation efficiency in the mineralization of phenol under UV illumination. A set of titania–silica mixed oxide materials was prepared by a cosolvent-induced gelation method. In this method, non-polar solvents, such as toluene, were used to modulate the hydrolysis of the alkoxide precursor. The hydrolysis of tetraethylorthosilicate is much slower in comparison to titanium tetraisopropoxide. This creates uncontrolled precipitation and poor dispersion of titania. Aromatic cosolvents, such as toluene, act as weak donor solvents for titanium alkoxide and slow down the hydrolysis process, hence allowing for hydrolysis rates of the starting two alkoxides to be similar. This allows for better dispersion of titania and

enhanced crystallinity over the silica support, as indicated in our previous study. The synthesized materials have been extensively characterized by using several techniques and utilized for phenol degradation under UV illumination. The degradation of phenol follows first-order kinetics, and the intermediates formed during the degradation process were qualitatively identified by using high-performance liquid Chromatography (HPLC) and atomic pressure chemical ionization mass spectroscopy (APCI-MS) techniques. In addition, the remnant total organic contents were also evaluated by Total Organic Carbon (TOC) measurements, and, thus, the complete removal of phenol was evidenced. Moreover, the formation of the highly reactive  $\bullet\text{OH}$  radical species was qualitatively elucidated by the fluorescence studies. We believe that this study provides the detailed guidance to understand the optimal structural property requirements for an efficient catalyst by comparing a set of materials prepared under similar experimental conditions with different titania–silica ratios.

## 2. Results and Discussion

The X-ray diffraction patterns of the mixed oxide materials prepared with different Ti:Si ratios of 1:4, 1:1, 2:1, and 3:1 and labelled as TS-25, TS-50, TS-67, and TS-75, respectively, show noticeable differences in diffraction peak intensities and explain the variation in the crystallinity of the materials. Figure 1 depicts the XRD patterns of the mixed oxide materials prepared in the presence of an ethanol–toluene solvent–cosolvent mixture along with the material that contains only titania (TS-100).

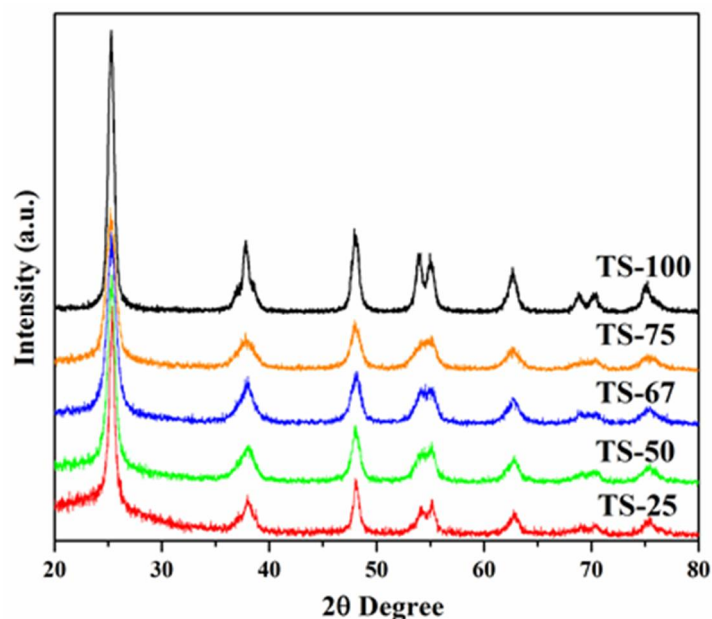


**Figure 1.** X-ray diffraction pattern of the  $\text{TiO}_2$ – $\text{SiO}_2$  mixed oxide system prepared with different Ti:Si ratio in the presence of ethanol–toluene solvent mixture.

The material TS-100 displays high-intensity peaks, suggesting the high crystallinity of the titania phase. In comparison to TS-100,  $\text{TiO}_2$ – $\text{SiO}_2$  mixed oxides materials show low diffraction contrast in the anatase phase of  $\text{TiO}_2$  due to the presence of amorphous silica. However, all the materials exhibit the peaks due to  $d_{101}$ ,  $d_{004}$ ,  $d_{200}$ ,  $d_{105}$ ,  $d_{211}$ ,  $d_{204}$ ,  $d_{116}$ , and  $d_{220}$  at  $2\theta$  values of  $25.5^\circ$ ,  $37.9^\circ$ ,  $48.3^\circ$ ,  $54.3^\circ$ ,  $55.2^\circ$ ,  $62.9^\circ$ ,  $69.1^\circ$ , and  $75.4^\circ$  degrees. These confirm that the  $\text{TiO}_2$ – $\text{SiO}_2$  mixed oxide materials contain  $\text{TiO}_2$  only in the anatase phase, and the increase in the silica amount resulted in the peak broadening in the final materials. Raman studies (figures are not shown here) further supported the presence of a pure anatase phase and the crystalline nature of the  $\text{TiO}_2$  phase. All samples display the peaks at  $638$ ,  $510$ ,  $391$ , and  $143\text{ cm}^{-1}$  for  $\text{TiO}_2$ . There was an additional shoulder at  $197\text{ cm}^{-1}$  observed in all Raman spectra, which may be due to the Eg symmetric modes.

Thus, both the XRD and Raman studies confirmed that the crystallinity of titania is affected by silica incorporation and also that the crystallite size of titania is altered depending on the silica amount. The crystallite sizes of titania in the mixed oxide materials are also affected by the incorporation of silica. The crystallite size of the pure  $\text{TiO}_2$  material was obtained using the Scherrer formula by considering the  $d_{101}$  peak, and it was found to be larger (12.6 nm), whereas the crystallite size of the other mixed oxide materials lies in the range of 8.1 to 11.1 nm. A decreasing trend was observed among the mixed oxide materials when the amount of silica decreases, which may be due to the variation in the dispersion of titania in the silica support. Further, TEM studies of the selected mixed oxide materials, TS-50, and TS-100, which have a 1:1 and 1:0 Ti:Si ratio, respectively, show the presence of lattice fringes due to the titania phase that is illustrated in Figure 2. The higher crystallinities of TS-100 than TS-50 indicate that the incorporation of silica lowers the crystallinity of the materials. In addition, the surface topography of the  $\text{TiO}_2$ - $\text{SiO}_2$  mixed oxide materials was recorded using Scanning Electron Microscopy (SEM), and representative images are shown in Figure S1 for TS-50 and TS-100. It was observed that the mixed oxide particles aggregate and form larger secondary particles micrometers in size.

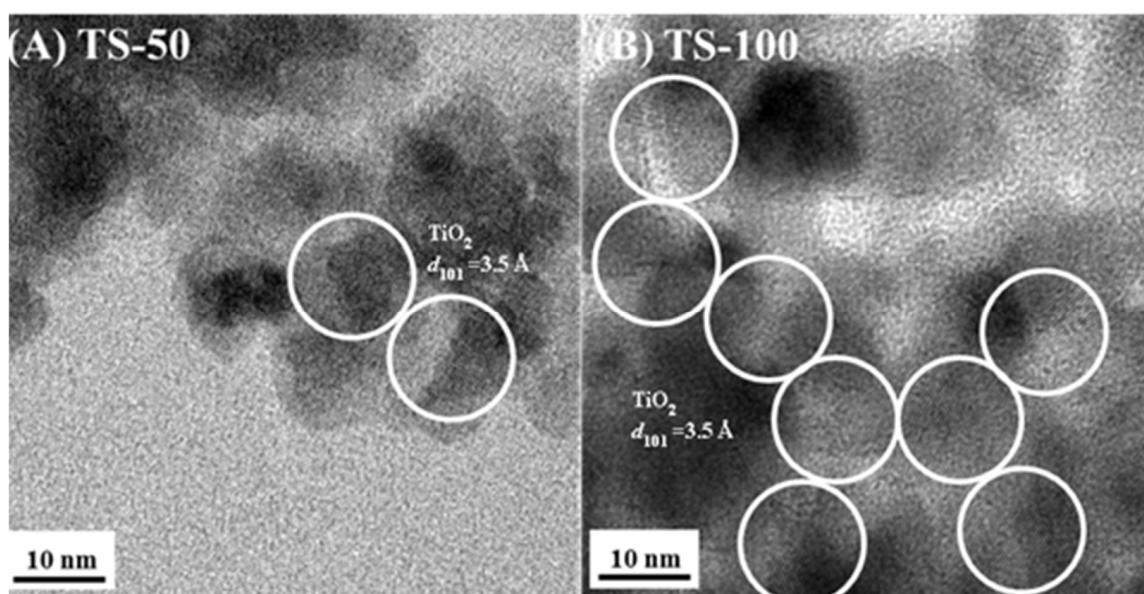


**Figure 2.** Transmission electron microscopic (TEM) image of the  $\text{TiO}_2$ - $\text{SiO}_2$  mixed oxide system with different (A) TS-50 (Ti:Si ratio of 1:1) and (B) TS-100 (Ti:Si ratio of 1:0) prepared in the presence of ethanol-toluene solvent mixture.

Although there was a lack of silica peaks in the mixed materials evidenced by the XRD patterns, the FT-IR analysis specifies the presence of heterolinkages in the materials (Figure 3). The bands at the wavenumbers of  $437$ ,  $579$ , and  $1027\text{ cm}^{-1}$  are due to the bending vibration of  $\text{Ti-O-Ti}$ ,  $\text{Si-O-Si}$  and the stretching frequency of  $\text{Si-O-Si}$ , respectively.

In addition, a shoulder is recorded at  $956\text{ cm}^{-1}$  and assigned to  $\text{Si-O-H}$  groups. Although the band in the region between  $930$  and  $960\text{ cm}^{-1}$  can be attributed to the presence of  $\text{Ti-O-Si}$  heterolinkages, pure silica materials also indicate a band at this region and confirm the presence of a  $\text{Si-O-H}$  group. A peak at  $783\text{ cm}^{-1}$  was observed, particularly in the pure  $\text{TiO}_2$  sample (TS-100) assigned to the  $\text{Ti-O}$  vibration, where the oxygen atom is in the non-bonding state [37].

The nitrogen isotherms of  $\text{TiO}_2$ - $\text{SiO}_2$  mixed oxides materials are shown in Figure 4A. All these materials exhibit the type IV isotherm, which is characteristic for the mesoporous materials taking place via multilayer adsorption followed by capillary condensation. Thus, initially the adsorption process is similar to the macroporous solids. Changes in hysteresis loops were observed in these mixed oxides, which may be due to the presence of a

different amount of silica. The materials TS-25, TS-50, and TS-67 show the hysteresis loop classification H3 that are typical for materials that consist of aggregates of plate-like particles forming slit-like pores. TS-75 exhibits parallel and horizontal branches, and this corresponds to the H4-type hysteresis loop.

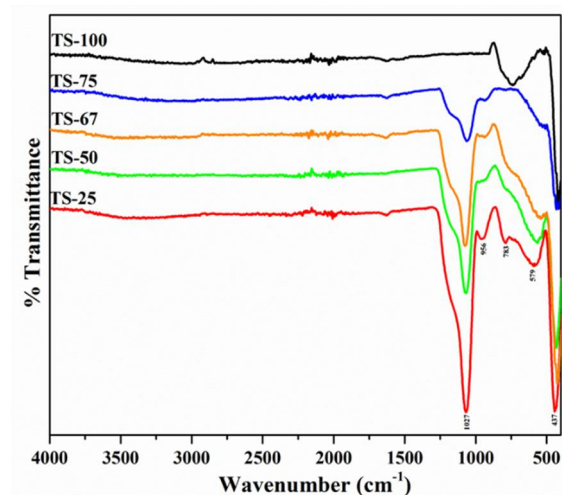


Figure 3. FT-IR spectrum of  $\text{TiO}_2\text{-SiO}_2$  mixed oxides prepared with different Ti:Si ratio in the presence of ethanol-toluene solvent mixture.

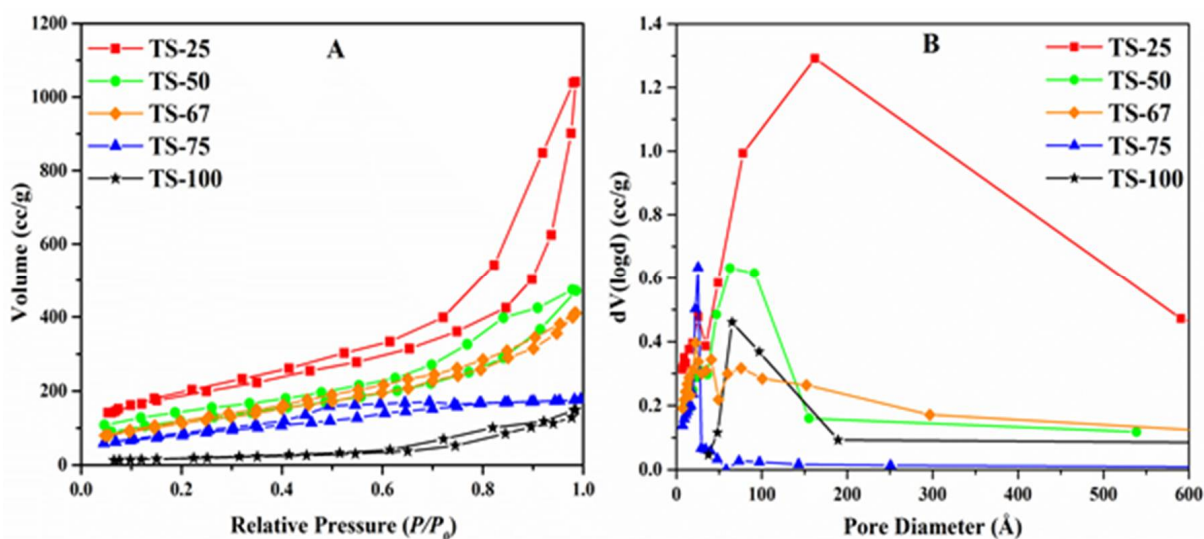
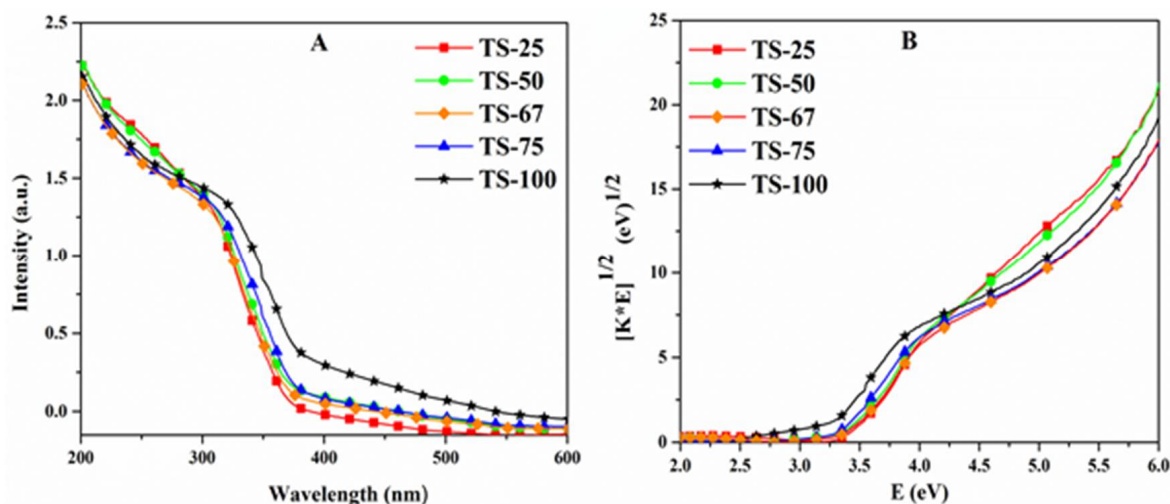


Figure 4. (A) Nitrogen isotherms of the  $\text{TiO}_2\text{-SiO}_2$  mixed oxides with different Ti:Si ratios (B) Pore size distributions of the materials.

It was observed that the surface area and pore volume of the mixed oxide materials increased with the increased amount of silica. The sample TS-25 exhibits a broad pore size distribution that is centered at  $\sim 164 \text{ \AA}$  with an additional peak at  $26 \text{ \AA}$  (Figure 4B). Thus, this material shows the pore diameter of  $96 \text{ \AA}$ , derived from the desorption branch of the nitrogen physisorption by applying the BJH equation. TS-50 also shows a broad pore size distribution, while the TS-67 results in a multimodal distribution with the pore size of  $62 \text{ \AA}$ . A fairly narrow and unimodal distribution at  $25 \text{ \AA}$  was obtained for the sample TS-75, and the unimodal center was shifted to a larger value for the pure  $\text{TiO}_2$  material TS-100. In addition, the peak for TS-100 was not found to be as sharp as the peak observed with the material TS-75, which may be due to the influence of silica in the TS-75 material and the effect of cosolvent in the pure  $\text{TiO}_2$  material, TS-100.

The absorbance spectra of the  $\text{TiO}_2\text{-SiO}_2$  mixed oxide materials were obtained using the UV-Visible diffuse reflectance spectroscopic analysis and are depicted in Figure 5A.

The electron transitions from the valence band to the conduction band of the materials were attained by the absorption below the wavelength of 400 nm. The band gap energies were calculated from the transformed Kubelka–Munk function versus the light energy plot, shown in Figure 5B. All the mixed oxide materials have the band gap in the range of 3.2 and 3.4 eV, similar to that of the pure TiO<sub>2</sub> bandgap energy. Table 1 illustrates all the structural properties of the materials along with the rate constants.



**Figure 5.** (A) The absorbance spectra of TiO<sub>2</sub>–SiO<sub>2</sub> mixed oxides with different Ti:Si ratios (B) Tauc plot obtained through the transformation of Kubelka–Munk function.

**Table 1.** Textural properties and rate of degradation of TiO<sub>2</sub>–SiO<sub>2</sub> mixed oxides prepared using different Ti:Si ratios.

Sample	% Ti	SSA (m <sup>2</sup> /g)	PV (cm <sup>3</sup> /g)	PD (Å)	Crystallinity (Intensity of <i>d</i> <sub>101</sub> )	Particle Size (nm)	Rate (×10 <sup>−4</sup> ) (s <sup>−1</sup> )
TS-25	25	672	1.61	96	610	2.7	4.59
TS-50	50	423	0.73	68	551	3.3	2.54
TS-67	67	409	0.64	62	505	3.2	2.41
TS-75	75	295	0.27	37	431	4.2	2.10
TS-100	100	65	0.23	141	729	ND	5.39

TS refers to titania–silica and the numbers convey the % amount of titania present in the materials. SSA refers to specific surface area, PV to pore volume, and PD to BJH pore diameter, which was determined by applying the BJH equation to the desorption isotherm.

### 2.1. Photocatalytic Degradation

A simple, toxic, and highly water-soluble (Solubility of 8.3 g/100 g of water at 20 °C) compound, phenol with an initial concentration of  $2 \times 10^{-4}$  M was chosen as a model pollutant. The quantification of the total remnant organics after irradiation was completed by TOC and HPLC analysis. More than 94% of total organic content removal was attained from the TOC analysis with all the mixed oxide materials, whereas a complete removal (100%) was achieved with the pure TiO<sub>2</sub> material, TS-100, at that time. It is well known that the photocatalytic activity of a semiconductor material is mainly dependent on surface and structural properties, such as crystal phase and composition, surface area, crystallite or particle size, porosity, band gap, and surface hydroxyl density.

In this study, it can be seen that the phenol degradation follows first-order kinetics, as illustrated in the normalized concentration plot (Figure 6A) and the kinetic plot (Figure 6B), where the concentration of phenol at time *t* is denoted as *C* and the initial concentration is noted as *C*<sub>0</sub>. The rate constants (Table 1) were obtained from the linear natural logarithmic

plot  $\ln(C/C_0)$  vs.  $t$  by considering its slope. Notably, surface area, pore volume, and the pore diameter of the materials seem to influence the degradation efficiency. The variation in the amount of silica present in the mixed oxide materials was found to alter the textural properties. A relatively high surface area of  $672 \text{ m}^2/\text{g}$  was recorded for the material, TS-25, prepared with high loading of silica (Ti:Si = 1:3). The high silica loading may provide better dispersion of titania crystallites, and this may be important for its ability to degrade phenol effectively in comparison to other titania–silica materials prepared in this study.

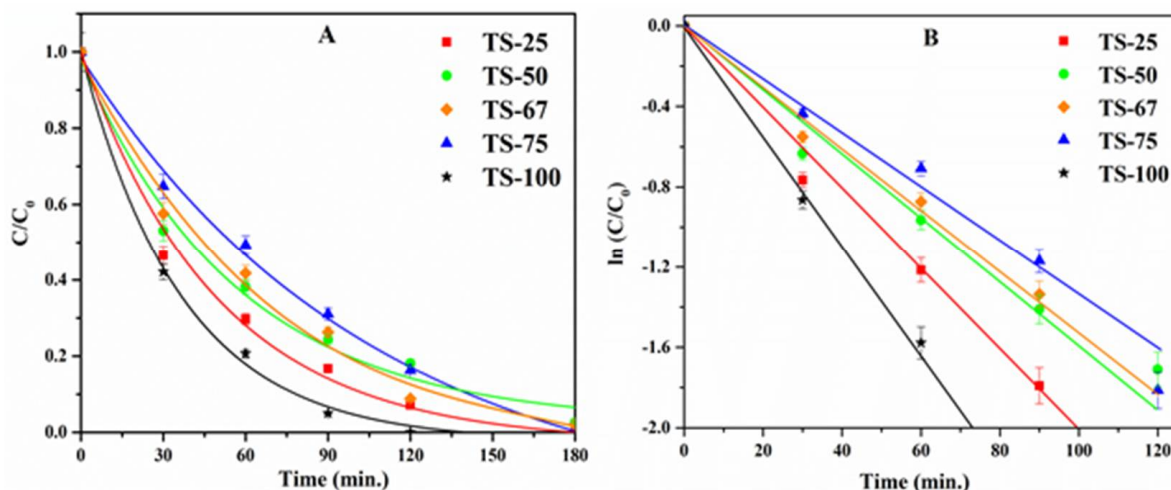


**Figure 6.** (A) Plot of  $C/C_0$  vs. time and (B) The plots of  $\ln(C/C_0)$  vs. time plots of  $\text{TiO}_2$ – $\text{SiO}_2$  mixed oxides with different Ti:Si ratios.

In addition, the high pore volume of  $1.61 \text{ cm}^3/\text{g}$ , and the larger pore diameter of  $96 \text{ \AA}$  could also be reasons for the higher activity of TS-25 in comparison to the other mixed titania–silica oxide materials used in this study. An increase in the amount of titania decreases the surface area of the mixed oxide materials from  $672 \text{ m}^2/\text{g}$  (TS-25) to  $295 \text{ m}^2/\text{g}$  (TS-75). Likewise, the pore volume and pore diameter also decrease as the amount of titania in the mixed oxides increases. Even though titania acts as an active photocatalytic site, the photocatalytic activity was found to decrease with an increase in loading of  $\text{TiO}_2$ . This may be attributed to the greater influence of textural properties such as surface area, pore volume, and pore diameter that effectively provide enhanced mass transport or effective molecular trafficking of reactants, intermediates, and products. In addition to the textural properties of these materials, formation of Ti–O–Si heterolinkages also modifies the  $\text{TiO}_2$ – $\text{SiO}_2$  interface and yields unique catalytic properties in the mixed oxide materials [38,39]. In order to understand the role of Ti–O–Si linkages, XPS studies were carried out. Figure 7 indicates the de-convoluted O 1s spectra.

The percentage of Ti–O–Si surface content was calculated from XPS analysis by using the procedure stated in the previous reports. Briefly, the O 1s transition was fit to two peaks near 530 eV [40] and 532 eV [41]. Then the broad bands between 530 and 532 eV were de-convoluted to three additional peaks. The Ti–O–Si species was quantified using Gaussian/Lorentzian shape GL (30:70) curves with equivalent electron volts (eV) at the full-width-half-maximum (fwhm) by considering the band near 531.7 eV [40,42,43]. Figure 7 shows the de-convoluted O 1s spectra of all  $\text{TiO}_2$ – $\text{SiO}_2$  materials prepared with different Ti:Si ratios and the calculated percentage of all the species, such as Ti–O–Si, Ti–O–Ti, Si–O–Si, Ti–O–H, and Si–O–H, which are listed in Table S1 in the supplementary section. It was noted that the percentage of Ti–O–Si species increases until the titania content increases up to 67% in the mixed oxide materials, and then it decreases with the further increase of titania. The increase in the Ti–O–Si heterolinkages from TS-25 to TS-67 may simply be attributed to an increase in the amount of titania in the mixed oxides. This is also supported by a concomitant increase in Ti–O–Ti and decrease in Si–O–Si bonds, as indicated in Table S1. Regarding the material, TS-75, the percentage of Ti–O–Si heterolinkage seems

lower in comparison to TS-67 and the reason for this observation may be due the difference in dispersion of titania in this material, driven by the synthesis method. These findings suggest no correlation between the Ti–O–Si linkage and the degradation efficiency in the mixed oxides prepared with different loadings of titania–silica. Thus, one needs to be cautious in linking the factors that impact the activity.

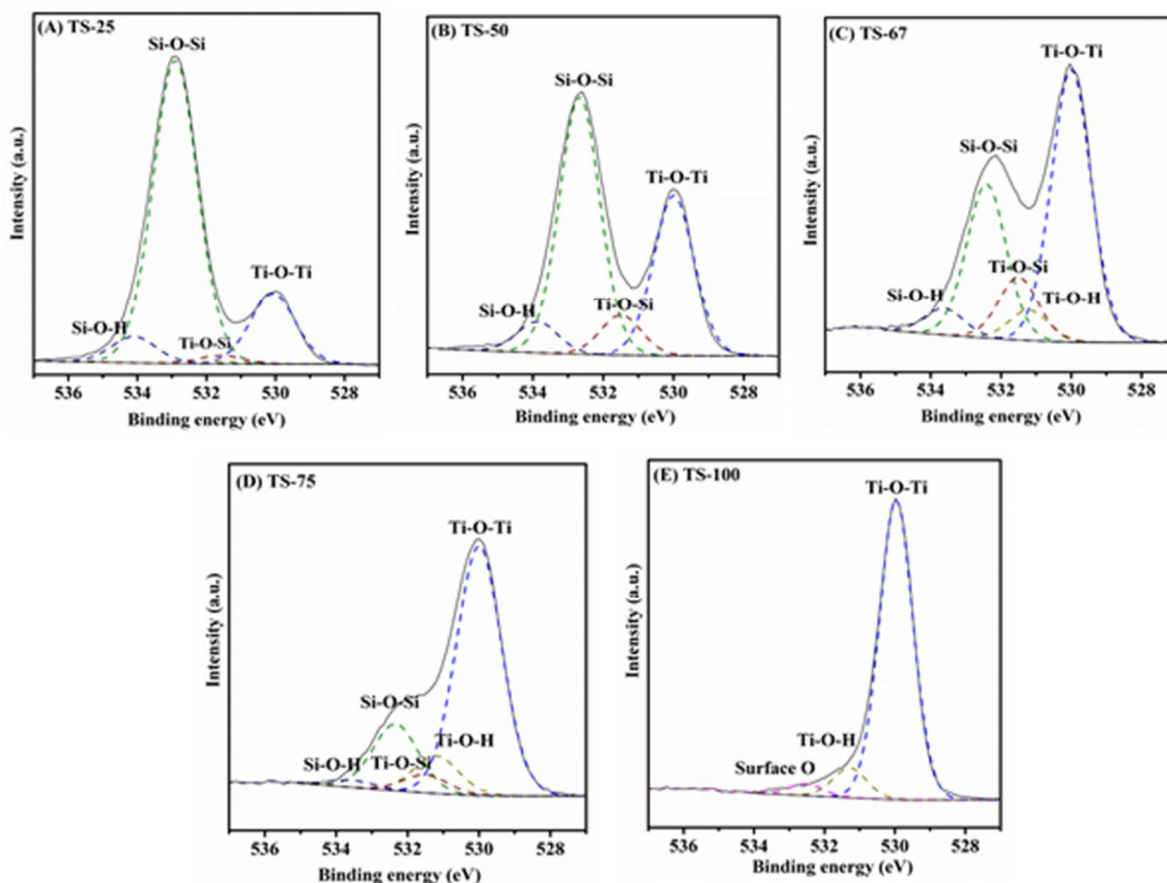


**Figure 7.** De-convoluted O 1S spectra of (A) TS-25, (B) TS-50, (C) TS-67, (D) TS-75, and (E) TS-100.

## 2.2. HPLC Analysis

There are several intermediates of degraded phenol that have toxicity in the environment reported in the existing literature [44]. In particular, the addition of hydroxyl radical resulted in hydroxy benzenes, and these intermediate species can further oxidize and lead to the highly substituted intermediates and the acidic intermediates after the cleavage of the ring [45–47]. The HPLC results provide a broader picture regarding the intermediates that formed under our experimental conditions, and it was further validated by the APCI-MS studies explained in the subsequent section. Notably, the di- (CC and HQ) and tri- (PG and HHQ) hydroxy benzenes were found to be the major intermediates. The keto-enol tautomerism of these hydroxy benzenes resulted in the intermediates HBQ and BQ. However, CC formation was found to be more favorable than HQ, and this may be due to the intramolecular hydrogen bonding between the ortho disubstituted hydroxyl groups on the benzene ring. Among the quinones that can be in equilibrium with the dihydroxy benzene products under acidic conditions, p-benzoquinone was identified as a dominant intermediate in our studies compared to o-benzoquinone, which implies instability of this intermediate in the aqueous medium [48].

Continuous attack of hydroxyl radicals in the primary intermediates results in ring-opening products that include Maleic acid (MA), Fumaric acid (FA), Oxalic acid (OA), Malonic acid (MAL), and Acetic acid (AA), which have been reported thus far as ring-opening products [46,47,49–52]. The observations for the formation of these isomeric forms

(MA and FA) were also confirmed by the mass spectroscopic characterization. In addition to MA and FA, there are some other acidic products identified by the APCI-MS studies elaborated in the following section. Furthermore, the solution mixture pH was recorded to be approximately seven after six hours of irradiation, and the neutral pH value supported the complete degradation and/or presence of mild acidic nature in the final solution. The quantitative calculations of the intermediates from the HPLC studies follow a Gaussian trend; moreover, all the samples prepared with different Ti/Si ratios have similar patterns during the degradation process.

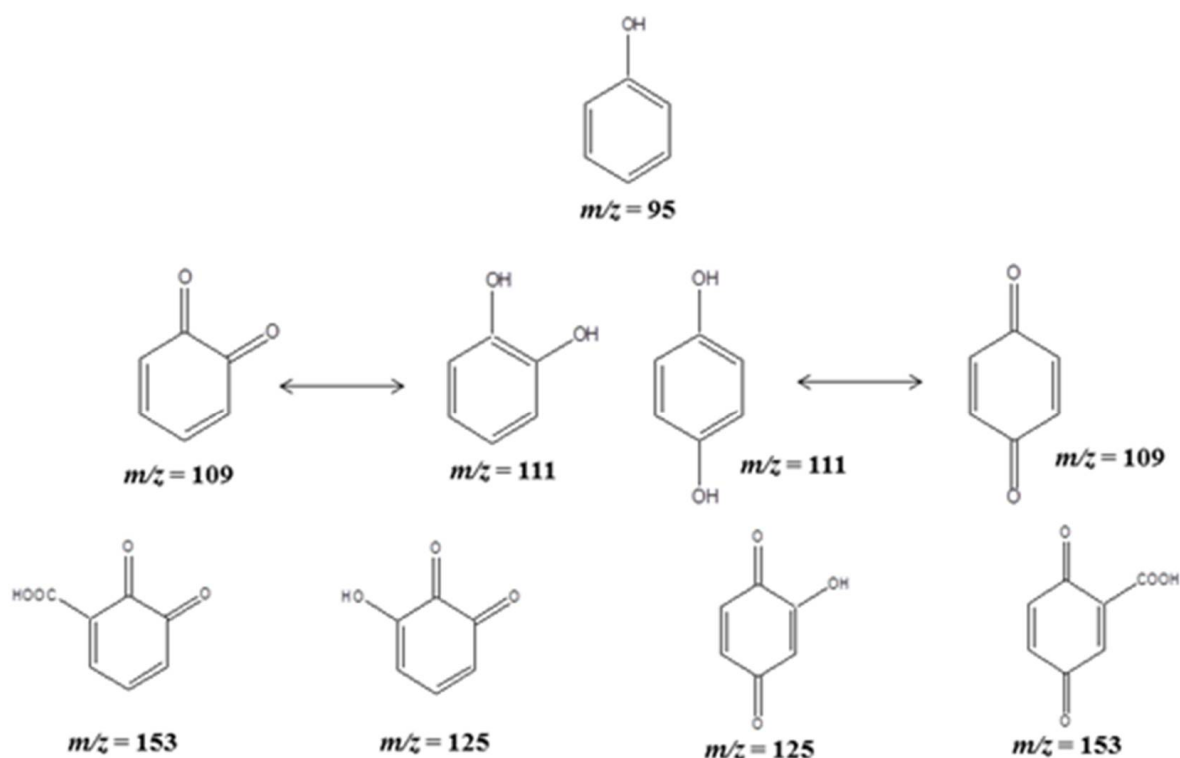
### 2.3. APCI-MS Analysis for the Fragmented Products

The MS analysis was carried out to identify the fragmented products of phenol with two selected mixed oxide catalysts, TS-50 and TS-100, which were prepared with a 1:1 and 1:0 Ti:Si ratio, respectively. The hydroxyl radical produced during the irradiation initiates the fragmentation of phenol. Even though several intermediates were identified according to their  $m/z$  values from the mass spectroscopic studies, the HPLC analysis could not detect all the intermediates obtained from the mass spectroscopy because of the detection limitations, as explained in the previous section. The major intermediates, which include CC, HQ, BQ, HBQ, and PG, were identified from the HPLC studies, and these intermediates were also detected in the MS analysis (Figures S2–S12).

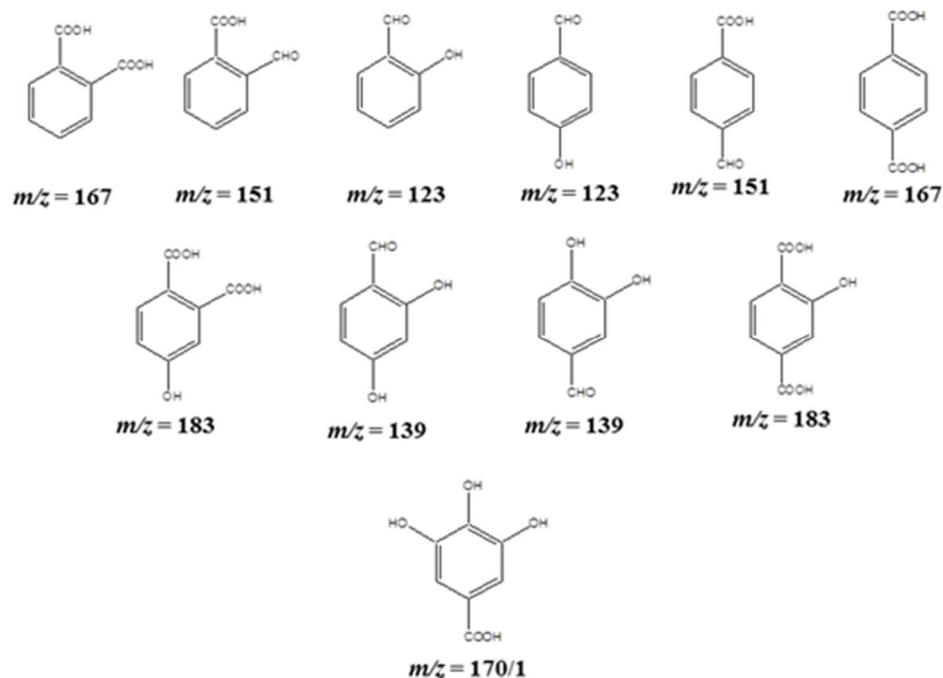
The mass spectrum for the initial phenol solution shows the peaks at  $m/z = 95$  (the parent peak), 77, and 59. This indicates that there is probably an autoionization in the parent molecule due to atomic pressure chemical ionization. The peak at  $m/z = 77$  belongs to the benzene ring, and the peak at  $m/z = 59$  recorded may be due to the formation of a  $C_2H_5CHOH$  molecular ion. Further, the UV irradiation resulted in several other peaks for the different intermediates because the addition of hydroxyl radical followed the keto-enol tautomerism, which formed carboxylated products from the oxidation.

HPLC studies indicated that CC formed as the most predominant intermediate compared to the HQ species. The peak detected at  $m/z = 111$  was due to the ortho, meta and/or para-attack of the  $\bullet OH$  radical, and the tautomerism gives the corresponding keto products of those hydroxy phenols at  $m/z = 109$ . However, it has been noted from the HPLC studies that there was no formation of resorcinol (RC) under our experimental conditions. Thus, the structures predicted herein for the  $m/z$  values of 111 and 109 have been only considered as ortho and para substitutions. An addition of  $\bullet OH$  radical on the benzoquinones resulted in hydroxy benzoquinones at  $m/z$  values of 125. Following oxidation, a peak ensued at  $m/z = 153$  for the di-oxo benzoic acid derivatives as intermediate products during the phenol degradation, as illustrated in Scheme 1.

In addition, the disubstituted intermediates, such as hydroxy benzaldehydes, formyl benzoic acids, and benzene dicarboxylic acids (ortho- and para-phthalic acid) were also detected at the  $m/z$  values of 123, 151, and 167, respectively, and are illustrated in Scheme 2. Even though all the plausible structures for the corresponding  $m/z$  values are listed herein, the ortho-substituted products are predicted to be the most favored ones due to the intramolecular hydrogen bonding between the ortho substitutions. In addition to the disubstituted products, formation of trisubstituted derivatives was also evidenced by the MS studies with the  $m/z$  values of 139 and 183. The  $m/z$  value of 139 may be due to the formation of dihydroxy benzoic acid derivatives, such as 2,4-dihydroxy benzoic acid and 3,4-dihydroxy benzoic acid. The hydroxy-benzene dicarboxylic acids (i.e., 2-hydroxy-1,4-benzenedicarboxylic acid, 4-hydroxy-1,2-benzenedicarboxylic acid, or 3-hydroxy-1,2-benzene dicarboxylic acid) form a peak at  $m/z = 183$ , and this may imply the formation of trisubstituted products due to the H-bonding between the carboxylic and hydroxy groups at the ortho positions. Nonetheless, trihydroxy benzene, i.e., pyrogallol, evidenced from the HPLC studies was not recorded in the mass spectroscopic study, but trihydroxy benzoic acid derivatives (i.e., Gallic acid or Phloroglucinol carboxylic acid) were detected as intermediatea at an  $m/z$  value of 170, as illustrated in Scheme 2.

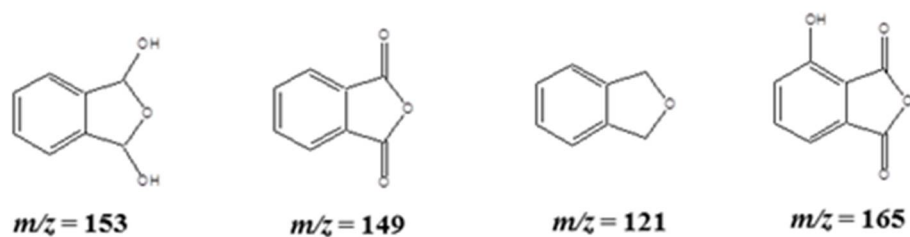


**Scheme 1.** The primary (Hydroxy and Quinone intermediates) fragmented products of phenol detected in APCI-MS analysis.



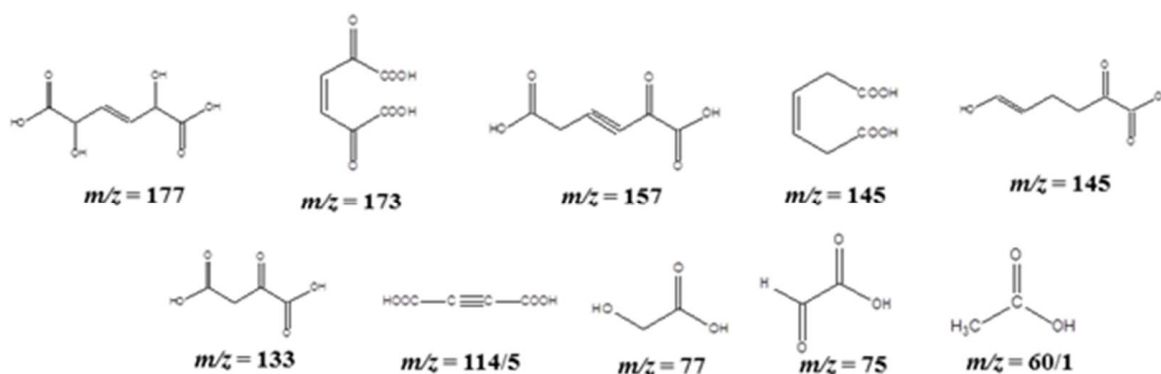
**Scheme 2.** The secondary (di- and trisubstituted) fragmented products of phenol detected in APCI-MS analysis.

The benzene dicarboxylic acid derivatives formed during the degradation products were followed by the formation of bicyclic products, and those were detected at  $m/z = 149$ ,  $165$ , and  $121$ , corresponding to the intermediate products (Scheme 3), which include phthalic anhydride, 3-hydroxyphthalic anhydride, and phthalane (1,3-dihydro-2-benzofuran), respectively.



**Scheme 3.** The possible bicyclic fragmented products of phenol detected in APCI-MS analysis.

Further, the attack with  $\bullet\text{OH}$  radicals resulted in ring-opening acid fragments (Scheme 4), such as 2,5-dihydroxy-3-hexenedioic acid ( $m/z = 177$ ), 2,5-dioxo-3-hexenedioic acid ( $m/z = 173$ ), 2-oxo-3-hexynedioic acid ( $m/z = 157$ ), 3-hexenedioic acid ( $m/z = 145$ ), 2,3-dihydroxyfumaric acid or 2,3-dihydroxymaleic acid ( $m/z = 149$ ), 2-oxosuccinic acid ( $m/z = 133$ ), fumaric acid or maleic acid ( $m/z = 117$ ), 2-butynedioic acid (acetylene dicarboxylic acid) ( $m/z = 114/5$ ), 2-hydroxyethanoic acid (glycolic acid) ( $m/z = 77$ ), 2-oxyethanoic acid (glyoxylic acid) ( $m/z = 75$ ), and acetic acid ( $m/z = 60/1$ ).



**Scheme 4.** The possible ring-opening fragmented products of phenol detected in APCI-MS analysis.

It is noteworthy to mention here that both selected catalysts show similar fragmented products in the mass spectroscopic analysis, and thus the formation of different intermediate products was found to depend on the formation of reactive oxygen species (ROS) during the irradiation. It is well known that in a heterogeneous photocatalysis the ROS play an important role in degrading the organics. To evaluate the formation of ROS,  $\bullet\text{OH}$  trapping experiments were carried out. These radicals can react with terephthalic acid (TPA) and form fluorescent 2-hydroxyterephthalic acid (2-HTPA). The formation of 2-HTPA is proportional to the amount of  $\bullet\text{OH}$  formed. Figure 8 shows a plot of fluorescence intensity for 2-HTPA vs. time for all the catalysts used in this study.

It can be seen from Figure 8 that the production of  $\bullet\text{OH}$  radical at the initial stage is high in the sample TS-100, which contains only  $\text{TiO}_2$ , and is followed by TS-25, TS-50, TS-67, and TS-75. A similar trend was observed until 80 min. of irradiation, and this may explain the differences in the rate of degradation. The sample TS-75 was found to produce lower amount of hydroxyl radicals, and it further supports its least activity among all the samples used in this study. These results suggest that the  $\bullet\text{OH}$  radicals play an important role in the phenol degradation, and the degradation of phenol was found to be highly affected by hydroxyl radicals generated by irradiation.

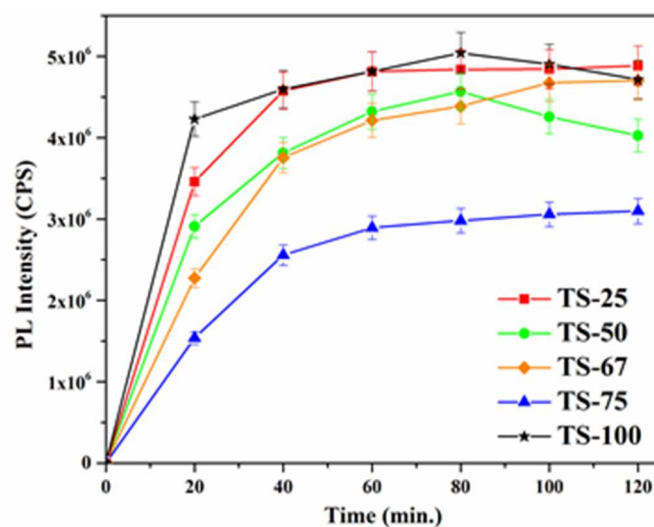


Figure 8. Plot of fluorescence intensity of 2-HTPA vs. time for TiO<sub>2</sub>-SiO<sub>2</sub> mixed oxide materials.

### 3. Materials and Methods

#### 3.1. Materials

Readily available Tetraethylorthosilicate (TEOS, Acros 98%), Titanium isopropoxide (Ti(<sup>i</sup>OPr)<sub>4</sub>, Acros 98+%), Anhydrous ethanol (Pharmco-AAPER, ACS/USP grade, 200 proof), toluene (ACS grade), and conc. nitric acid (HNO<sub>3</sub>) were used as received for the preparation of the TiO<sub>2</sub>-SiO<sub>2</sub> mixed oxides. Commercially available Phenol (Acros, Waltham, MA, USA, ACS Grade, 99+%), hydroquinone (Sigma, St. Louis, MO, USA >99%), benzoquinone (TCI America, Gardena, CA, USA 98%), Maleic acid (Alfa Aesar, Tewksbury, MA, USA), Acetic acid (Fisher), Fumaric acid (Acros), Pyrogallol (Alfa Aesar, ACS Grade, 99%), Catechol, and methanol (Acros, Waltham, MA, USA 99.9% HPLC grade) were used without further purification. Nano pure water (resistivity > 18 mΩ.cm) was used to prepare the solution mixtures. Terephthalic acid (TPA, Acros, Waltham, MA, USA, 98%) was used as received for the scavenging experiments.

#### 3.2. Synthesis of TiO<sub>2</sub>-SiO<sub>2</sub> Mixed Oxides

TiO<sub>2</sub>-SiO<sub>2</sub> mixed oxides with different TiO<sub>2</sub>:SiO<sub>2</sub> molar ratios (1:4, 1:1, 2:1, and 3:1) were prepared by simultaneous hydrolysis and condensation of TEOS and Ti(<sup>i</sup>OPr)<sub>4</sub> in the presence of an ethanol-toluene solvent-cosolvent combination by following a procedure similar to that previously reported by us [30]. The blank titania sample (TS-100) was obtained by the hydrolysis and condensation of Ti(<sup>i</sup>OPr)<sub>4</sub> in the presence of an ethanol-toluene solvent mixture. The obtained gels were then hydrothermally treated at 120 °C for 12 h. Finally, the mixed oxide powders were ground and calcined by heating in static air at 500 °C for 6 h with the heating rate of 3 °C/min. The resultant samples were then named as TS-25 (1:4), TS-50 (1:1), TS-67 (2:1), TS-75 (3:1), and TS-100 (blank Titania), respectively.

#### 3.3. Characterization

The TiO<sub>2</sub>-SiO<sub>2</sub> mixed oxides were characterized by using several techniques. Powder X-ray diffraction patterns were recorded at room temperature on a Rigaku Ultima IV instrument with Cu Kα radiation (λ = 1.5408 Å) and with 40 kV accelerating voltage, 44 mA emission current, and two theta angles (2θ) from 20° to 80° with 0.02° step size and 1°/min. scan rate. The obtained diffraction patterns were analyzed using PDXL software provided by Rigaku. A Quantachrome Nova 2200e surface area analyzer was used for the nitrogen physisorption studies. The samples were dried overnight at 70 °C prior to the analysis, followed by an extensive degassing at 100 °C, and then N<sub>2</sub> adsorption-desorption isotherms were recorded at 77 K. The Brunauer-Emmett-Teller (BET) equation was used to calculate the surface area within the relative pressure P/P<sub>0</sub> range of 0.05–0.30. The

pore volume was obtained from the nitrogen amount adsorbed at the highest relative pressure  $P/P_0 \approx 0.99$ . The pore diameter and pore size distribution plots were determined by applying the Barrett–Joyner–Halenda (BJH) model to the desorption isotherm. The synthesized mixed oxides were further analyzed by using Scanning Electron Microscopy (SEM, FEI 450) and Transmission Electron Microscopy (TEM, Hitachi H-7000FA). SEM images were typically recorded at 20 kV and  $2 \times 10^{-6}$  Torr. The TEM images were recorded on a Hitachi H-7000 FA instrument operating at 100 kV. The samples (~5 mg) were first dispersed in ethanol (~20 mL) by sonication for 10 to 15 min. The dispersed solution (2 to 3 drops) was deposited on C film-coated Cu TEM grids (200 mesh) and allowed to air-dry overnight prior to the TEM analysis. Raman spectra were obtained with a Horiba Jobin Yvon LabRamARAMIS spectrophotometer with an internal HENE (633 nm) excitation laser. The unfiltered beam of scattered laser radiation was focused onto the sample through a microscope objective ( $\times 50$ ) for an acquisition time of 10 s and repetition of  $10\times$ . The radiation was then dispersed by an 1800 line/mm grating onto the CCD detector. The diffuse reflectance spectra (DRS) spectra of the samples were recorded in the range of 200–800 nm using a Cary 100 Bio UV-Vis spectrophotometer equipped with a Harrick DR praying mantis accessory. Fourier Transform-Infrared (FT-IR) spectra of the  $\text{TiO}_2$ – $\text{SiO}_2$  mixed oxide materials were recorded using a Bruker instrument model ALPHA equipped with an ATR platinum diamond module of spectral range capabilities from 50,000–50  $\text{cm}^{-1}$ . The crystal type is automatically recognized by the spectroscopy software OPUS 6.5 and optimal measurements were obtained at 24 scans with a resolution of 4  $\text{cm}^{-1}$ . X-ray Photoelectron Spectroscopy (XPS) studies were carried out using a custom-designed Kratos Axis Ultra system to interpret the chemical environment of the oxide species present on the surface of the photocatalysts. Survey scans were collected with the following parameters: energy scan range of 1200 to 25 eV, pass energy of 160 eV, and the step size of 1 eV. High-resolution spectra were attained in the region with an energy window of 20–40 eV, pass energy of 20 eV, and step size of 0.1 eV. The absolute energy scale was calibrated to the C 1s peak at a binding energy of 284.6 eV, since this minimizes any errors in sample charging effects. The deconvolution of the XPS peaks was completed using CASA XPS software, and a Tougaard-type background was subtracted from each spectrum to minimize the scattered electron noise.

### 3.4. Photo Degradation

The photocatalytic activity of the mixed oxide materials was carried out in the following procedure. An appropriate amount of  $\text{TiO}_2$ – $\text{SiO}_2$  mixed oxide materials was dissolved in  $2 \times 10^{-4}$  M phenol in a quartz cylindrical jacket reactor to make a 1 mg/mL suspension. The initial pH of the solution was recorded in the range of 4 to 6. The suspension was purged with molecular oxygen (60 mL/min) and stirred at 300 rpm in the dark for 30 min. to establish the adsorption–desorption equilibrium. The reaction temperature was kept constant at  $25 \pm 2$  °C by routing water between the double-wall reactor. After 30 min, the Xenon lamp (Newport 1000 W) was turned on to provide the irradiation through a Pyrex glass filter cut of 280 nm. These experimental conditions were maintained throughout the whole experiment. Of the reaction mixture, 15 mL was withdrawn in 30 min. time periods, and it was centrifuged at 3200 rpm for 15 min. Finally, it was filtered through a 0.45  $\mu\text{m}$  Millipore filter membrane and the clear filtrate was used for analysis.

### 3.5. Analytical Techniques

The obtained filtrate was immediately tested using a Shimadzu TOC-V CSH total organic carbon analyzer and High-Performance Liquid Chromatography (HPLC) in a SP8800/8810 LC Pump equipped with a Spectra 100 UV-Vis detector to explore the catalytic activity of  $\text{TiO}_2$ – $\text{SiO}_2$  mixed oxide materials. A reversed phase C18 5  $\mu$ , 250 mm length and 4.6 mm internal diameter column was used for the separation of reactant and the intermediates. A mixture of 40% methanol and 60% deionized water with 1% glacial acetic acid was used as the mobile phase and argon gas was purged into the mobile phase to

minimize the auto-oxidation of the products. The mobile phase was infused at a rate of 1.0 mL/min and the detection wavelength was kept at 254 nm. The reaction intermediates were confirmed by the coinjection of the commercial standards at the same operating conditions. Quantities of the intermediates were calculated by using the calibration plots of maleic acid (MA), fumaric acid (FA), pyrogallol (PG), hydroquinone (HQ), catechol (CC), benzoquinone (BQ), and phenol (PhOH). The stock solutions of these samples were prepared in the concentration of  $2 \times 10^{-4}$  M and serial dilution was made to prepare the test solution in the range from  $1.25 \times 10^{-5}$  M to  $2 \times 10^{-4}$  M for the calibration plot. The BQ calibration plot was used to find the quantity of hydroxy benzoquinone (HBQ), due to the unavailability of the HBQ standard.

The Varian 500-MS Ion Trap Mass Spectrometer was used for the identification of the degraded products of phenol during the photocatalysis process. Ionization was completed by an atomic pressure chemical ionization (APCI) source in positive mode to separate the fragments on the basis of their mass-to-charge ratio ( $m/z$ ). The test samples were infused in the rate of  $100 \mu\text{Lmin}^{-1}$ , whereas the other parameters were kept as follows: Spray shield voltage = 600 V, Capillary voltage = 80 V, Needle voltage = 5000 V, Drying gas temperature =  $400^\circ\text{C}$ , Nebulizer pressure = 10 psi, and the electron multiplier voltage = 1360 V. The peak pattern was recorded in the  $m/z$  range of 50–200.

### 3.6. Scavenging Experiment

The amount of  $\bullet\text{OH}$  formed on the surface of TS materials was evaluated by applying the fluorescence technique. Terephthalic acid (TPA) was used as a fluorescence trap for the  $\bullet\text{OH}$  radicals. It is well known that the  $\bullet\text{OH}$  radicals react readily with TPA to produce highly fluorescent 2-hydroxyterephthalic acid. In a typical experiment, 20 mg of photocatalyst were added into  $5 \times 10^{-4}$  M TPA solution prepared in  $2 \times 10^{-3}$  M NaOH. The suspension was stirred well in the dark for 20 min, and then the suspension was irradiated with UV light. Every 20 min, 5 mL aliquots were drawn and filtered through a  $0.45 \mu\text{m}$  Millipore filter membrane. Finally, the clear solution was analyzed for fluorescence emission intensity of the 2-hydroxyterephthalic acid with the excitation wavelength at 315 nm. The intensity of the peak at 425 nm was predicted to be proportional to the amount of  $\bullet\text{OH}$  formed.

## 4. Conclusions

Highly active  $\text{TiO}_2\text{-SiO}_2$  mixed oxides have been successfully synthesized by the hydrothermal synthesis through a cosolvent-induced gelation method. During the photocatalysis process, the illumination of a titania–silica ( $\text{TiO}_2\text{-SiO}_2$ ) semiconductor catalyst with ultraviolet (UV) radiation activates the catalyst, creating a redox environment, which is necessary for degradation. The cosolvents facilitate dispersion of anatase in the silica framework. The textural properties of the titania–silica mixed oxides seemed to play an important role. The proposed mechanism of this degradation process proceeds through the CC pathway, and there is a small contribution from the HQ pathway. Our mechanism provides the evidence for the formation of CC, HQ, BQ, HBQ, and PG as major intermediates. In addition, MA and FA were found as minor intermediates during the degradation process. TOC and LC results suggest that phenol is converted into  $\text{CO}_2$  and  $\text{H}_2\text{O}$ . This study provides guidance regarding intermediates formed during the degradation of PhOH using these mixed oxide catalysts.

**Supplementary Materials:** The following supporting information can be downloaded at: <https://www.mdpi.com/article/10.3390/catal12020193/s1>, Table S1. The percentage surface contents of  $\text{TiO}_2\text{-SiO}_2$  mixed oxide materials; Figure S1: Scanning electron microscopic (SEM) image of the  $\text{TiO}_2\text{-SiO}_2$  mixed oxide system with different (A) TS-50 (Ti:Si ratio of 1:1) and (B) TS-100 (Ti:Si ratio of 1:0) prepared in the presence of ethanol–toluene solvent mixture; Figure S2: APCI-MS Spectrum of pure Phenol; Figure S3: APCI-MS Spectrum of phenol under dark condition with the catalyst TS-50; Figure S4: APCI-MS Spectrum of phenol after 1h of irradiation with the catalyst TS-50; Figure S5: APCI-MS Spectrum of phenol after 2 h of irradiation with the catalyst TS-50; Figure S6: APCI-MS

Spectrum of phenol after 3 h of irradiation with the catalyst TS-50; Figure S7: APCI-MS Spectrum of phenol after 6 h of irradiation with the catalyst TS-50; Figure S8: APCI-MS Spectrum of phenol under dark condition with the catalyst TS-100; Figure S9: APCI-MS Spectrum of phenol after 1 h of irradiation with the catalyst TS-100; Figure S10: APCI-MS Spectrum of phenol after 2 h of irradiation with the catalyst TS-100; Figure S11: APCI-MS Spectrum of phenol after 3 h of irradiation with the catalyst TS-100; Figure S12: APCI-MS Spectrum of phenol after 6 h of irradiation with the catalyst TS-100.

**Author Contributions:** Conceptualization, S.Y. and R.T.K.; methodology, S.Y.; software, S.Y. and C.-M.W.; validation, S.Y.; formal analysis, S.Y. and C.-M.W.; investigation, S.Y.; resources, S.Y. and R.T.K.; data curation, S.Y.; writing—original draft preparation, S.Y.; writing—review and editing, R.T.K.; visualization, S.Y.; supervision, R.T.K.; project administration, R.T.K.; funding acquisition, R.T.K. All authors have read and agreed to the published version of the manuscript.

**Funding:** We extend sincere gratitude to NSF-CHE-0619190, NSF-CHE-0722632, NSF-EPS-0903804, DE-EE0000270, NNX12AB17G, and the state of SD for funding this project.

**Data Availability Statement:** Not applicable.

**Conflicts of Interest:** The authors declare no conflict of interest.

## References

1. Bahnemann, D. Photocatalytic water treatment: Solar energy applications. *Sol. Energy* **2004**, *77*, 445–459. [[CrossRef](#)]
2. Vidal, A. Developments in solar photocatalysis for water purification. *Chemosphere* **1998**, *36*, 2593–2606. [[CrossRef](#)]
3. Schröder, H.F. Pollutants in drinking water and waste water. *J. Chromatogr. A* **1993**, *643*, 145–161. [[CrossRef](#)]
4. Barceló, D. Environmental Protection Agency and other methods for the determination of priority pesticides and their transformation products in water. *J. Chromatogr. A* **1993**, *643*, 117–143. [[CrossRef](#)]
5. Tyas, M.J. A histochemical study of the effect of phenol on the mitochondria and lysosomes of cultured cells. *Histochem. J.* **1978**, *10*, 333–342. [[CrossRef](#)] [[PubMed](#)]
6. Beloborodova, N.; Bairamov, I.; Olenin, A.; Shubina, V.; Teplova, V.; Fedotcheva, N. Effect of phenolic acids of microbial origin on production of reactive oxygen species in mitochondria and neutrophils. *J. Biomed. Sci.* **2012**, *19*, 89. [[CrossRef](#)] [[PubMed](#)]
7. Michałowicz, J.; Duda, W. Phenols—Sources and toxicity. *Pol. J. Environ. Stud.* **2007**, *16*, 347–362.
8. Tian, L.H.; Liu, H.T.; Gao, Y. Degradation and adsorption of rhodamine B and phenol on TiO<sub>2</sub>/MCM-41. *Kinet. Catal.* **2012**, *53*, 554–559. [[CrossRef](#)]
9. Rasalingam, S.; Peng, R.; Koodali, R.T. An investigation into the effect of porosities on the adsorption of rhodamine B using titania–silica mixed oxide xerogels. *J. Environ. Manag.* **2013**, *128*, 530–539. [[CrossRef](#)]
10. Kibombo, H.S.; Rasalingam, S.; Koodali, R.T. Facile template free method for textural property modulation that enhances adsorption and photocatalytic activity of aperiodic titania supported silica materials. *Appl. Catal. B-Environ.* **2013**, *142*, 119–128. [[CrossRef](#)]
11. Guo, N.; Liang, Y.; Lan, S.; Liu, L.; Ji, G.; Gan, S.; Zou, H.; Xu, X. Uniform TiO<sub>2</sub>–SiO<sub>2</sub> hollow nanospheres: Synthesis, characterization and enhanced adsorption–photodegradation of azo dyes and phenol. *Appl. Surf. Sci.* **2014**, *305*, 562–574. [[CrossRef](#)]
12. Brigante, M.; Schulz, P.C. Adsorption of paraquat on mesoporous silica modified with titania: Effects of pH, ionic strength and temperature. *J. Colloid Interface Sci.* **2011**, *363*, 355–361. [[CrossRef](#)] [[PubMed](#)]
13. Xu, Y.; Lebrun, R.E.; Gallo, P.-J.; Blond, P. Treatment of textile dye plant effluent by nanofiltration membrane. *Sep. Sci. Technol.* **1999**, *34*, 2501–2519. [[CrossRef](#)]
14. Won, S.W.; Choi, S.B.; Chung, B.W.; Park, D.; Park, J.M.; Yun, Y.S. Biosorptive decolorization of reactive orange 16 using the waste biomass of *Corynebacterium glutamicum*. *Ind. Eng. Chem. Res.* **2004**, *43*, 7865–7869. [[CrossRef](#)]
15. Chong, M.N.; Jin, B.; Chow, C.W.K.; Saint, C. Recent developments in photocatalytic water treatment technology: A review. *Water Res.* **2010**, *44*, 2997–3027. [[CrossRef](#)]
16. Honglan, S.; Xiaoliang, C.; Qihua, W.; Ruipu, M.; Yinfa, M. Assessment and removal of emerging water contaminants. *J. Environ. Anal. Toxicol.* **2012**, *2*, 1–14.
17. Riegel, G.; Bolton, J.R. Photocatalytic efficiency variability in TiO<sub>2</sub> particles. *J. Phys. Chem.* **1995**, *99*, 4215–4224. [[CrossRef](#)]
18. Zou, J.; Gao, J. H<sub>2</sub>O<sub>2</sub>-sensitized TiO<sub>2</sub>/SiO<sub>2</sub> composites with high photocatalytic activity under visible irradiation. *J. Hazard. Mater.* **2011**, *185*, 710–716. [[CrossRef](#)]
19. Shifu, C.; Gengyu, C. Photocatalytic degradation of organophosphorus pesticides using floating photocatalyst TiO<sub>2</sub>·SiO<sub>2</sub>/beads by sunlight. *Sol. Energy* **2005**, *79*, 1–9. [[CrossRef](#)]
20. Marugán, J.; López-Muñoz, M.-J.; Gernjak, W.; Malato, S. Fe/TiO<sub>2</sub>/pH interactions in solar degradation of imidacloprid with TiO<sub>2</sub>/SiO<sub>2</sub> photocatalysts at pilot-plant scale. *Ind. Eng. Chem. Res.* **2006**, *45*, 8900–8908. [[CrossRef](#)]
21. Mahyar, A.; Behnajady, M.A.; Modirshahla, N. Enhanced photocatalytic degradation of CI Basic Violet 2 using TiO<sub>2</sub>–SiO<sub>2</sub> composite nanoparticles. *Photochem. Photobiol.* **2011**, *87*, 795–801. [[CrossRef](#)]

22. Aguado, J.; van Grieken, R.; López-Muñoz, M.-J.; Marugán, J. A comprehensive study of the synthesis, characterization and activity of TiO<sub>2</sub> and mixed TiO<sub>2</sub>/SiO<sub>2</sub> photocatalysts. *Appl. Catal. A: Gen.* **2006**, *312*, 202–212. [[CrossRef](#)]
23. Davis, R.J.; Liu, Z. Titania-silica: A model binary oxide catalyst system. *Chem. Mater.* **1997**, *9*, 2311–2324. [[CrossRef](#)]
24. Cetinkaya, T.; Neuwirthová, L.; Kutláková, K.M.; Tomášek, V.; Akbulut, H. Synthesis of nanostructured TiO<sub>2</sub>/SiO<sub>2</sub> as an effective photocatalyst for degradation of acid orange. *Appl. Surf. Sci.* **2013**, *279*, 384–390. [[CrossRef](#)]
25. Malinowska, B.; Walendziewski, J.; Robert, D.; Weber, J.V.; Stolarski, M. The study of photocatalytic activities of titania and titania-silica aerogels. *Appl. Catal. B Environ.* **2003**, *46*, 441–451. [[CrossRef](#)]
26. Ismail, A.A.; Ibrahim, I.A.; Ahmed, M.S.; Mohamed, R.M.; El-Shall, H. Sol-gel synthesis of titania-silica photocatalyst for cyanide photodegradation. *J. Photochem. Photobiol. A Chem.* **2004**, *163*, 445–451. [[CrossRef](#)]
27. Klein, S.; Thorimbert, S.; Maier, W.F. Amorphous microporous titania-silica mixed oxides: Preparation, characterization, and catalytic redox properties. *J. Catal.* **1996**, *163*, 476–488. [[CrossRef](#)]
28. Anderson, C.; Bard, A.J. An improved photocatalyst of TiO<sub>2</sub>/SiO<sub>2</sub> prepared by a sol-gel synthesis. *J. Phys. Chem.* **1995**, *99*, 9882–9885. [[CrossRef](#)]
29. Hutter, R.; Mallat, T.; Baiker, A. Titania silica mixed oxides: II. Catalytic behavior in olefin epoxidation. *J. Catal.* **1995**, *153*, 177–189. [[CrossRef](#)]
30. Kibombo, H.S.; Zhao, D.; Gonshorowski, A.; Budhi, S.; Koppang, M.D.; Koodali, R.T. Cosolvent-induced gelation and the hydrothermal enhancement of the crystallinity of titania-silica mixed oxides for the photocatalytic remediation of organic pollutants. *J. Phys. Chem. C* **2011**, *115*, 6126–6135. [[CrossRef](#)]
31. Rasalingam, S.; Kibombo, H.S.; Wu, C.-M.; Budhi, S.; Peng, R.; Baltrusaitis, J.; Koodali, R.T. Influence of Ti-O-Si hetero-linkages in the photocatalytic degradation of Rhodamine B. *Catal. Commun.* **2013**, *31*, 66–70. [[CrossRef](#)]
32. Rasalingam, S.; Kibombo, H.S.; Wu, C.-M.; Peng, R.; Baltrusaitis, J.; Koodali, R.T. Competitive role of structural properties of titania-silica mixed oxides and a mechanistic study of the photocatalytic degradation of phenol. *Appl. Catal. B Environ.* **2014**, *148–149*, 394–405. [[CrossRef](#)]
33. Xu, N.P.; Shi, Z.F.; Fan, Y.Q.; Dong, J.H.; Shi, J.; Hu, M.Z.C. Effects of particle size of TiO<sub>2</sub> on photocatalytic degradation of methylene blue in aqueous suspensions. *Ind. Eng. Chem. Res.* **1999**, *38*, 373–379. [[CrossRef](#)]
34. Takeda, N.; Torimoto, T.; Sampath, S.; Kuwabata, S.; Yoneyama, H. Effect of inert supports for titanium dioxide loading on enhancement of photodecomposition rate of gaseous propionaldehyde. *J. Phys. Chem.* **1995**, *99*, 9986–9991. [[CrossRef](#)]
35. Torimoto, T.; Ito, S.; Kuwabata, S.; Yoneyama, H. Effects of adsorbents used as supports for titanium dioxide loading on photocatalytic degradation of propylamide. *Environ. Sci. Technol.* **1996**, *30*, 1275–1281. [[CrossRef](#)]
36. Alemany, L.J.; Banares, M.A.; Pardo, E.; Martin, F.; Galán-Fereres, M.; Blasco, J. Photodegradation of phenol in water using silica-supported titania catalysts. *Appl. Catal. B Environ.* **1997**, *13*, 289–297. [[CrossRef](#)]
37. Vasconcelos, D.C.L.; Costa, V.C.; Nunes, E.H.M.; Sabioni, A.C.S.; Gasparon, M.; Vasconcelos, W.L. Infrared spectroscopy of titania sol-gel coatings on 316L stainless steel. *Mater. Sci. Appl.* **2011**, *2*, 1375–1382. [[CrossRef](#)]
38. Kooyman, P.; Waal, P.; Verdaasdonk, P.J.; Jansen, K.; Bekkum, H. Titanium deposited from TiCl<sub>4</sub> on amorphous silica and silicalite-1 as catalyst in aromatic hydroxylation reactions. *Catal. Lett.* **1992**, *13*, 229–238. [[CrossRef](#)]
39. Anderson, C.; Bard, A.J. Improved photocatalytic activity and characterization of mixed TiO<sub>2</sub>/SiO<sub>2</sub> and TiO<sub>2</sub>/Al<sub>2</sub>O<sub>3</sub> materials. *J. Phys. Chem. B* **1997**, *101*, 2611–2616. [[CrossRef](#)]
40. Erdem, B.; Hunsicker, R.A.; Simmons, G.W.; Sudol, E.D.; Dimonie, V.L.; El-Aasser, M.S. XPS and FTIR surface characterization of TiO<sub>2</sub> particles used in polymer encapsulation. *Langmuir* **2001**, *17*, 2664–2669. [[CrossRef](#)]
41. Fukushima, M.; Zhou, Y.; Yoshizawa, Y.-I.; Hirao, K. Water vapor corrosion behavior of porous silicon carbide membrane support. *J. Eur. Ceram. Soc.* **2008**, *28*, 1043–1048. [[CrossRef](#)]
42. Kim, M.J.; Kim, K.-D.; Seo, H.O.; Luo, Y.; Dey, N.K.; Kim, Y.D. Improvement in the photocatalytic activity of TiO<sub>2</sub> by the partial oxidation of the C impurities. *Appl. Surf. Sci.* **2011**, *257*, 2489–2493. [[CrossRef](#)]
43. Wang, J.; Liu, X.; Li, R.; Qiao, P.; Xiao, L.; Fan, J. TiO<sub>2</sub> nanoparticles with increased surface hydroxyl groups and their improved photocatalytic activity. *Catal. Commun.* **2012**, *19*, 96–99. [[CrossRef](#)]
44. Gaya, U.I.; Abdullah, A.H.; Zainal, Z.; Hussein, M.Z. Photocatalytic degradation of 2, 4-dichlorophenol in irradiated aqueous ZnO suspension. *Int. J. Chem.* **2010**, *2*, 180–193. [[CrossRef](#)]
45. Zenkevich, I.G.; Kochetova, M.V.; Larionov, O.G.; Revina, A.A. Retention indices as the best reproducible chromatographic parameters for the characterization of phenolic compounds in reversed-phase high-performance liquid chromatography. *J. Anal. Chem.* **2005**, *60*, 655–667. [[CrossRef](#)]
46. Theurich, J.; Lindner, M.; Bahnemann, D.W. Photocatalytic degradation of 4-chlorophenol in aerated aqueous titanium dioxide suspensions: A kinetic and mechanistic study. *Langmuir* **1996**, *12*, 6368–6376. [[CrossRef](#)]
47. Devlin, H.R.; Iestyn, H.J. Mechanism of the oxidation of aqueous phenol with dissolved oxygen. *Ind. Eng. Chem. Fundam.* **1984**, *23*, 387–392. [[CrossRef](#)]
48. Alnaizy, R.; Akgerman, A. Advanced oxidation of phenolic compounds. *Adv. Environ. Res.* **2000**, *4*, 233–244. [[CrossRef](#)]
49. Gopalan, S.; Savage, P.E. Reaction mechanism for phenol oxidation in supercritical water. *J. Phys. Chem.* **1994**, *98*, 12646–12652. [[CrossRef](#)]
50. Chen, J.; Eberlein, L.; Langford, C.H. Pathways of phenol and benzene photooxidation using TiO<sub>2</sub> supported on a zeolite. *J. Photochem. Photobiol. A Chem.* **2002**, *148*, 183–189. [[CrossRef](#)]

- 
51. Zazo, J.A.; Casas, J.A.; Mohedano, A.F.; Gilarranz, M.A.; Rodríguez, J.J. Chemical pathway and kinetics of phenol oxidation by Fenton's reagent. *Environ. Sci. Technol.* **2005**, *39*, 9295–9302. [[CrossRef](#)] [[PubMed](#)]
  52. Guo, Z.; Ma, R.; Li, G. Degradation of phenol by nanomaterial TiO<sub>2</sub> in wastewater. *Chem. Eng. J.* **2006**, *119*, 55–59. [[CrossRef](#)]